https://dx.doi.org/10.1016/j.apenergy.2022.119046

Coupling deep learning and multi-objective genetic algorithms to achieve high performance and durability of direct internal reforming solid oxide fuel cell

Yang Wang[a,b], Chengru Wu[a,b], Siyuan Zhao[b], Jian Wang[b], Bingfeng Zu[c], Minfang Han[d], Qing Du[a,*], Meng Ni[b,*], Kui Jiao[a,*]

[a] State Key Laboratory of Engines, Tianjin University,

135 Yaguan Road, Tianjin, China

[b] Department of Building and Real Estate, Research Institute for Sustainable Urban Development (RISUD) & Research Institute for Smart Energy (RISE),

Hong Kong Polytechnic University, Hung Hom, Kowloon, Hong Kong, China

[c] Internal Combustion Engine Research Institute, Tianjin University, 92 Weijin Road, Tianjin, China

[d] Department of Energy and Power Engineering, Tsinghua University, Beijing, Beijing, 100084, China

Abstract

Direct internal reforming (DIR) operation of solid oxide fuel cell (SOFC) reduces system complexity, improves system efficiency but increases the risk of carbon deposition which can reduce the system performance and durability. In this study, a novel framework that combines a multi-physics model, deep learning, and multi-objective optimization algorithms is proposed for improving SOFC performance and minimizing carbon deposition. The sensitive operating parameters are identified by performing a global sensitivity analysis. The results of parameter analysis highlight the effects of overall temperature distribution and methane flux on carbon deposition. It is also found that the reduction of carbon deposition is accompanied by a decrease in cell performance. Besides, it is found that the coupling effects of electrochemical and chemical reactions cause a higher temperature gradient. Based on the parametric simulations, multi-objective optimization is conducted by applying a deep learning-based surrogate model

as the fitness function. The optimization results are presented by the Pareto fronts under different temperature gradient constraints. The Pareto optimal solution set of operating points allows a significant reduction in carbon deposition while maintaining a high power density and a safe maximum temperature gradient, increasing cell durability. This novel approach is demonstrated to be powerful for the optimization of SOFC and other energy conversion devices.

Keywords: Solid oxide fuel cell; Carbon deposition; Deep learning; Multi-objective optimization; Global sensitivity analysis

Nomenclature

c_p	specific heat capacity, kJ kg^{-1} K^{-1}
D	gas diffusivity, m^2 s^{-1}
E_{eq}	open circuit voltage, V
F	faraday's constant, C mol^{-1}
J	electrochemical reaction rate, A m^{-3} s^{-1}
K	permeability, m^2
j_0	exchange current density, A m^{-3}
n_e	number of electrons transferred per reaction
p	gas pressure, Pa or atm
P	power density, W m^{-2}
R	universal gas constant, J mol^{-1} K^{-1}
R_B	Boudouard reaction rate, $\times 10^{-6}$mol g_{cat}^{-1} s^{-1}
R_{MC}	methane cracking reaction rate, $\times 10^{-6}$mol g_{cat}^{-1} s^{-1}

S	source term, kg m^{-3} s^{-1}, mol m^{-3} s^{-1} or W m^{-3}
S_i	Sobol sensitivity index
T	temperature, K
V	variance
x	mole fraction
y	mass fraction

Greek letters

α	transfer coefficient in anode
φ_{ele}	electric potential, V
φ_{ion}	ionic potential, V
γ	adjustable parameter
η	overpotential, V
κ	thermal conductivity, W m^{-1} K^{-1}
σ	conductivity, S m^{-1}
μ	viscosity, kg m^{-1} s^{-1}
v	velocity, m s^{-1}
ρ	density, kg m^{-3}

Subscripts and superscripts

a	anode
act	activation
avg	average

c	cathode
eff	effective
ele	electron
f	fluid
grad	gradient
i	gas species
ion	ion
m	reaction order
ohm	ohmic
op	operating
out	output
s	solid

Abbreviations

ANN	artificial neural network
CDR	carbon deposition rate
DIR	direct internal reforming
DL	deep learning
DNN	deep neural network
GSA	global sensitivity analysis
MOGA	multi-objective genetic algorithm
MSR	methane steam reforming reaction

RMSE	root-mean square error
R^2	squared correlation coefficient
SOFC	solid oxide fuel cell
S/M	steam/methane ratio
WGS	water gas shift

1. Introduction

Growing concerns over fossil fuel shortages and environmental issues have led to widespread interest in new environmental-friendly power generation technologies [1]. Among these technologies, the Solid Oxide Fuel Cells (SOFCs) enable a direct transformation of the chemical energy of the fuel into electricity and heat by the high-efficiency electrochemical reactions [2]. The high operating temperature (600-1000 ℃) confers SOFCs an advantage of being the most attractive subsystem of combined heat and power systems [3].

The Ni-based composite exhibits high electrocatalytic activity and has good thermal and chemical stability, thus becoming the most commonly used anode material [4]. The Ni phase is also a good catalyst for a variety of internal reforming reactions, while the high temperature can facilitate the cleavage of chemical bonds. This gives SOFCs excellent fuel flexibility and also offers the possibility for direct internal reforming (DIR) of hydrocarbon fuels [5], i.e., methane. The DIR can significantly reduce the total cost and complexity of the SOFC systems. As the heat generated by SOFC can be effectively utilized for endothermic reforming reaction occurring in the anode, the DIR also helps improve the SOFC system overall efficiency. But at the same time, the use of hydrocarbon fuels can cause carbon deposition in the SOFC anode, which may block the passage for gas transport or even destroy the anode structure, degrading the SOFC performance and durability. For methane fueled SOFCs, two main carbon deposition

reactions are involved inside the anode:

$$CH_4 \rightleftarrows C+2H_2 \text{ (Methane cracking)} \quad (1)$$

$$2CO \rightleftarrows C+CO_2 \text{ (Boudouard reaction)} \quad (2)$$

According to the typical operating conditions of SOFCs, the amorphous carbon is the most possible form of carbon deposition [6]. As the amount of carbon deposition increases, a carbon film can be formed on the surface of Ni catalyst and cover the electrochemical active sites, which will result in severe performance degradation. In recent years, substantial research has been conducted on alleviating the impact of carbon deposition [7-10]. Several constructive strategies have been proposed, including the development of carbon-resistant anode materials by replacing Ni-based catalyst with perovskite oxides or by modifying/doping the Ni-based catalysts [7,8], adding a mix-conducting interlayer between electrolyte and anode [9], and using a separate on-cell catalyst reforming layer on the top of the support layer [10].

In addition to the material and structure optimizations, the easiest and most cost-effective strategy is to identify proper operating conditions with a low risk of carbon deposition [11]. Adding a large amount of steam to hydrocarbon fuels to achieve a large steam/carbon ratio (S/C) and lowering the operating temperature have been proven to efficiently inhibit carbon deposition [12]. Suitable operating conditions are one of the necessary prerequisites to suppress carbon deposition and improve cell performance. Some studies have used numerical approaches such as thermodynamic analysis to qualitatively characterize the carbon deposition process [13-17]. The C-H-O ternary diagram is often used to determine the carbon deposition boundary of SOFCs fueled with hydrocarbons [13]. Muramoto et al. [14] systematically constructed the C-H-O diagrams of high-pressure SOFCs and determined the carbon deposition regions under high operating pressure. Subotić et al. [15] depicted the carbon deposition boundary considering different forms of carbon formation in the C-H-O diagram. In addition,

carbon activity is often used as an important indicator to assess whether carbon deposition can occur or not [16,17]. However, the above methods can only qualitatively predict the possibility of carbon deposition and cannot be used as a tool for quantitative optimization.

Generally speaking, there is a trade-off between cell durability and performance, and the same is true for carbon deposition. Increasing S/C and reducing operating temperature is not favorable for maintaining high cell performance and system efficiency, so optimization work must be performed under conditions that take into account both cell performance and carbon deposition. However, this type of optimization is challenging by experimental investigation, considering the time and cost involved in extensive experimental testing. For comparison, numerical approaches are very powerful tools for SOFCs performance prediction and parameter optimization, e.g., a large number of multi-scale models have been developed and used for design optimization at microstructure level [18], single-cell or stack level [19-21], and system-level [22,23]. Numerical studies have also been carried out on the catalytic reactors [24,25] and DIR-SOFC, such as applying Generalized Least Squares method to study methane/steam reforming kinetics [26], developing a transient model to study the transient response of reforming reactions inside cell [27], stablishing a microstructure-oriented mathematical model to investigate the muti-physics transport phenomena at a microscopic perspective [28]. However, these approaches are usually computationally intensive and challenging to achieve multi-objective optimization of cell performance and carbon deposition as described above. Combining multi-physics models with relevant data-driven algorithms such as machine learning and genetic algorithms can be an effective methodology [29]. For example, some studies have employed genetic algorithms to reformers to achieve optimal catalyst distribution [30], improve efficiency [31] and reduce carbon deposition [32]. However, no such optimization of parameters for achieving both high performance and durability of direct internal reforming SOFC (DIR-SOFC) can be found in the literature.

In this paper, a novel optimization framework is proposed for improving the electrochemistry and carbon deposition performance of DIR-SOFC. This framework combines multiple numerical methods, such as the multi-physics model, machine learning algorithm, global sensitivity analysis (GSA), and multi-objective genetic algorithm (MOGA). The experimentally validated multi-physics model comprehensively considers the internal heat and mass transfer process as well as chemical and electrochemical reactions. The dataset generated by the multi-physics model is used to train a deep neural network (DNN) to get a surrogate model. Then the global sensitivity analysis is performed to find the most sensitive operating parameters. Finally, the MOGA with constraint-handling strategy is applied to find the optimal trade-off between cell output performance and carbon deposition under a certain temperature gradient. This optimization process can also be applied to the performance optimization of a wide range of energy conversion devices.

2. Methods

2.1 Framework for the DIR-SOFC optimization

Fig. 1 shows the optimization flowchart for cell performance and carbon deposition. First, by comprehensively considering the internal heat and mass transfer processes as well as chemical and electrochemical reactions, a multi-physics model of DIR-SOFC is developed to obtain the cell performance under different operating conditions. Next, the validated physical model is used to perform the parametrical analysis and to generate the datasets for training the deep learning-based surrogate model. The trained deep neural network can accurately characterize the relationship between inputs (operating conditions) and outputs (cell performance parameters). Then the surrogate model is integrated into a sensitivity analysis algorithm to identify the significance of operating conditions. Meanwhile, a multi-objective optimization is carried out by setting the surrogate model as a fitness function to obtain the optimum trade-off solution that maximizes cell performance and minimizes the risk of carbon deposition.

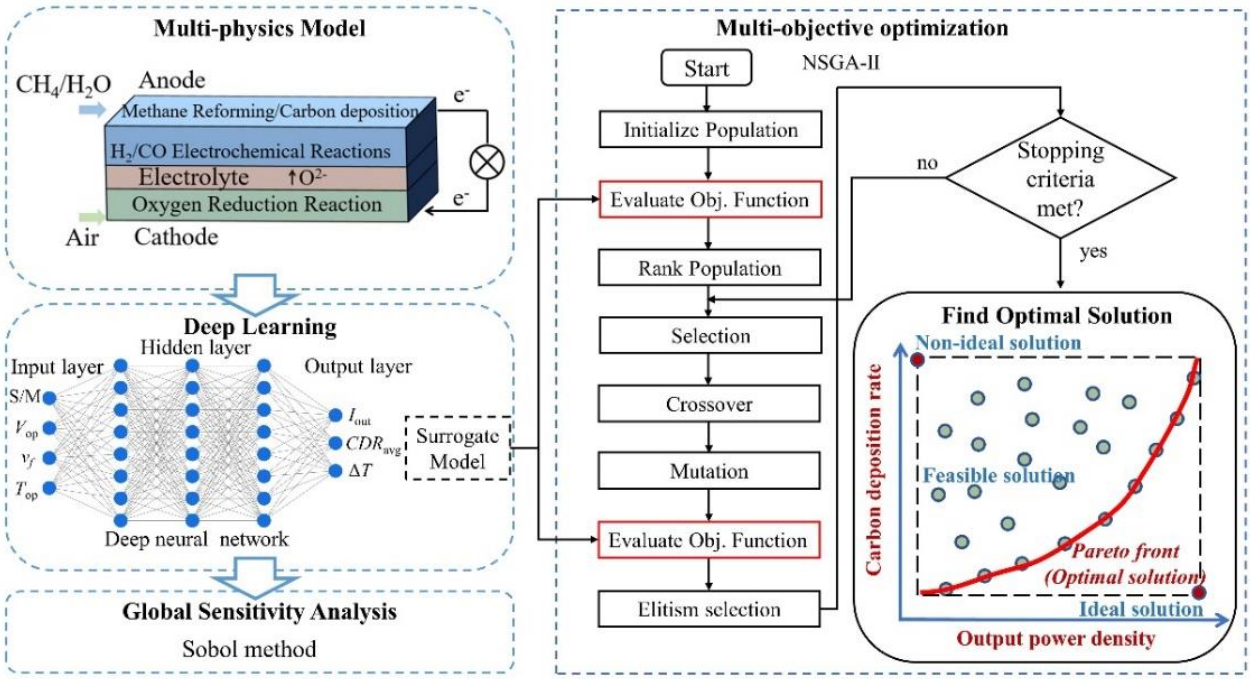

Fig. 1. Optimization flowchart for the electrochemistry and carbon deposition performance of DIR-SOFC

2.2 Multi-physics model development

The planar anode-supported SOFC is the optimal cell configuration at the present stage. The Ni-based cermet composites have excellent catalytic activity for internal reforming reactions of hydrocarbon fuels. At the three-phase boundary of the anode, the reforming reaction products (H_2 and CO) will simultaneously react with the oxygen ions produced by the cathode oxygen reduction reaction, generating electricity, heat, and gas products. A two-dimensional multi-physics SOFC model is developed, and the parameters of geometry and electrodes are listed in Table 1 [33].

Table 1. Cell parameters.

Parameters	Value
Cell length (mm)	80

Channel height (mm)	2
Anode support layer thickness (μm)	570
Anode functional layer thickness (μm)	30
Electrolyte thickness (μm)	15
Cathode thickness (μm)	30
Electrode (anode and cathode) porosity	0.4
Electrode (anode and cathode) permeability (m^2)	1.18e-12
Electrode (anode and cathode) tortuosity	3
Volume fraction of electron conductor	0.5
Electric conductivity of anode (S m^{-1}) [33]	$4.2\times10^{7}T^{-1}\exp(-1200T^{-1})$
Electric conductivity of cathode (S m^{-1}) [33]	$9.5\times10^{7}T^{-1}\exp(-1150T^{-1})$
Ionic conductivity (S m^{-1}) [33]	$6.92\times10^{4}\exp(-9681T^{-1})$

2.2.1 Conservation equations

The multi-physics model comprehensively considers the momentum, heat, and mass transfer as well as the electron/ion transfer processes. The corresponding conservation equations are summarized in Table 2. Among them, the widely used dusty gas model is used to characterize the multi-component diffusion process inside the porous anode. The equations used to calculate the effective parameters in the porous media are also listed in Table 2. The detailed expressions of effective diffusion coefficients and other related parameters can be found in [19].

Table 2. Governing equations.

Description	Governing equations	Computational domains
Mass	$\nabla\cdot(\rho v)=S_{\mathrm{m}}$	Channels, Electrodes

	$\rho(v\cdot\nabla)v=\nabla\cdot\left[-p+\mu\left(\nabla v+(\nabla v)^{\mathrm{T}}\right)\right]$	Channels
Momentum	$\frac{\rho}{\varepsilon}(v\cdot\nabla)\frac{v}{\varepsilon}=\nabla\cdot\left[-p+\frac{\mu}{\varepsilon}\left(\nabla v+(\nabla v)^{\mathrm{T}}\right)-\frac{2}{3}\frac{\mu}{\varepsilon}(\nabla\cdot v)\right]-\mu K^{-1}v$	Electrodes
Species	$\nabla\cdot\left(-\rho y_{\mathrm{i}}\sum_{\mathrm{j}\neq\mathrm{i}}^{\mathrm{n}}D_{\mathrm{eff,ij}}\nabla x_{\mathrm{j}}+\rho v y_{\mathrm{i}}\right)=S_{\mathrm{i}}$	Channels, Electrodes
Energy	$\nabla\cdot\left(\rho c_{\mathrm{p}}vT\right)=\nabla\cdot\left(\kappa_{\mathrm{eff}}\nabla T\right)+S_{\mathrm{T}}$	All domains
Electronic charge	$0=\nabla\cdot\left(\sigma_{\mathrm{ele}}^{\mathrm{eff}}\nabla\varphi_{\mathrm{ele}}\right)+S_{\mathrm{ele}}$	Electrodes
Ionic charge	$0=\nabla\cdot\left(\sigma_{\mathrm{ion}}^{\mathrm{eff}}\nabla\varphi_{\mathrm{ion}}\right)+S_{\mathrm{ion}}$	Electrodes, Electrolyte
Effective parameters		
Effective diffusion coefficient (D_{eff})	$D_{\mathrm{eff}}=\frac{\varepsilon}{\tau}\left(\frac{\sum_{\mathrm{j}\neq\mathrm{i}}\frac{x_{\mathrm{j}}}{D_{\mathrm{ij}}}}{1-x_{\mathrm{j}}}+\frac{1}{D_{\mathrm{k,ij}}}\right)^{-1}$	Porous electrodes
Effective thermal conductivity (κ_{eff})	$\kappa_{\mathrm{eff}}=(1-\varepsilon)\kappa_{\mathrm{s}}+\varepsilon\kappa_{\mathrm{f}}$	Porous electrodes
Effective electron/ion conductivity (σ_{eff})	$\sigma_{\mathrm{eff}}=\left(\frac{1-\varepsilon}{\tau}\right)\sigma_0$	Porous electrodes

2.2.2 Chemical model and carbon formation

The chemical reactions of DIR-SOFC include a series of heterogeneous reaction kinetics. The methane steam reforming (MSR) and water gas shift (WGS) reactions take a leading part in these reactions as follows:

$$CH_4 + H_2O \rightarrow CO+3H_2 \ \text{(MSR)} \tag{3}$$

$$H_2O+CO \rightarrow CO_2+H_2 \ \text{(WGS)} \tag{4}$$

The reaction kinetics of these two reactions are implemented into the multi-physics model. The detailed reaction rates expressions of MSR and WGS can be expressed as [34,35]:

$$R_{\mathrm{MSR}} = k_{\mathrm{rf}}\left(p_{\mathrm{CH_4}} p_{\mathrm{H_2O}} - \frac{p_{\mathrm{CO}}\left(p_{\mathrm{H_2}}\right)^3}{K_{\mathrm{pr}}} \right) \tag{5}$$

$$R_{\mathrm{WGS}} = k_{\mathrm{sf}}\left(p_{\mathrm{H_2O}} p_{\mathrm{CO}} - \frac{p_{\mathrm{H_2}} p_{\mathrm{CO_2}}}{K_{\mathrm{ps}}} \right) \tag{6}$$

where R_{MSR} and R_{WGS} (mol m^{-3} s^{-1}) are the reaction rates of methane steam reforming reaction and water gas shift reaction, respectively. k_{rf}/k_{sf} are the forward reaction constants, and K_{pr}/K_{ps} are the equilibrium constants.

One of the objectives of this work is to minimize carbon deposition without significantly decreasing cell performance. Two carbon formation pathways are considered to be the main sources of Ni-based anode coking: methane cracking reaction and Boudouard reaction, as given in Eqs. (1) and (2). The carbon activity has been used in many studies as a criterion to assess the possibility of carbon deposition [16,17]. However, it has been pointed out that the actual carbon deposition rate is not a function of carbon activity [36]. In the present study the equations based on chemical reaction kinetics are used to calculate the carbon deposition rate [36,37]:

$$R_{\mathrm{MC}} = p_{\mathrm{H_2}}^2 (\exp(-12516.98T^{-1}+0.26416)\cdot\frac{p_{\mathrm{CH_4}}}{p_{\mathrm{H_2}}^2} - \exp(-13024.01T^{-1}-0.00317)) \tag{7}$$

$$R_{\mathrm{B}} = p_{\mathrm{CO}}(-\exp(-11093.005T^{-1}-2.178)\cdot\frac{p_{\mathrm{CO_2}}}{p_{\mathrm{CO}}^2} + \exp(-3595.868T^{-1}-11.692)) \tag{8}$$

where R_{MC} and R_{B} ($\mathrm{mol\ g_{cat}^{-1}\ s^{-1}}$) are the reaction rates of methane cracking and Boudouard reaction, respectively. It is important to note that these reaction rates are only used to evaluate the magnitude of carbon deposition and are not included as the chemical reaction source terms

in the multi-physics model.

2.2.3 Electrochemical model

H_2 and CO are the main products of internal reforming reactions, which can directly participate in the electrochemical reactions:

$$\begin{aligned} &H_2 + O^{2-} \rightarrow H_2O + 2e^- \\ &CO + O^{2-} \rightarrow CO_2 + 2e^- \\ &\frac{1}{2}O_2 + 2e^- \rightarrow O^{2-} \end{aligned} \tag{9}$$

The electrons generated in the anode flow through the external circuit to the cathode to produce electric current. By assuming a constant voltage operation, the relationship between output voltage (V), equilibrium potential (E_{eq}), and overpotentials (η) can be expressed as:

$$V = E_{eq} - \eta_{act} - \eta_{ohm} \tag{10}$$

where η_{act} and η_{ohm} (V) are the activation overpotential and the ohmic overpotential, respectively. η_{act} can be calculated as: $\eta_{act} = \varphi_{ele} - \varphi_{ion} - E_{eq}$. φ_{ele} and φ_{ion} are the electric potential and electrolyte potential, respectively. η_{ohm} is determined by Ohm's law. When H_2 or CO is used as fuel, the equilibrium potentials can be expressed as [34]:

$$\begin{aligned} E_{eq,H_2} &= 1.253 - 0.00024516T + \frac{RT}{2F}\ln\left[\frac{p_{H_2}(p_{O_2})^{0.5}}{p_{H_2O}}\right] \\ E_{eq,CO} &= 1.46713 - 0.0004527T + \frac{RT}{2F}\ln\left[\frac{p_{CO}(p_{O_2})^{0.5}}{p_{CO_2}}\right] \end{aligned} \tag{11}$$

The electrochemical reaction rates (J, A m^{-3} s^{-1}) can be calculated by adopting the Butler-Volmer equation:

$$J = j_0\left(\exp\left(\alpha\frac{n_e F}{RT}\eta_{act}\right) - \exp\left(-(1-\alpha)\frac{n_e F}{RT}\eta_{act}\right)\right) \tag{12}$$

$$j_0 = \frac{\gamma_i RT}{n_e F}\left(\frac{p_i}{p_{ref,i}}\right)^m \exp\left(-\frac{E_{act}}{RT}\right) \tag{13}$$

where j_0 (A m^{-3}) is the exchange current density, γ_i is the prefactor for species i. Since the

electrochemical oxidation activity of H_2 is higher than that of CO, the prefactor of H_2 is set to 2.2 times that of CO [34].

2.2.4 Numerical procedure

The related coupled equations are implemented in COMSOL Multiphysics which discretizes the partial differential equations using the finite element method. The solving process is performed with the built-in PARDISO direct solver with advantages in multiprocessing architecture. For boundary conditions, the velocity inlet and the pressure outlet are used as boundary conditions for the momentum equation, while the inlet is set to the operating temperature and the external boundary other than the outlet is set to adiabatic. For electric potential solving, the upper boundary of the anode is set to the ground, the lower boundary is set to the operating voltage, and the rest is set to electrical insulation.

Meanwhile, the model validation on the multi-physics model is performed while maintaining the operating conditions, cell materials, and geometrical parameters consistent with the experiment [38]. As shown in Fig. 2(a), the polarization curves obtained from simulation results fit well with the experimental data at different operating temperatures.

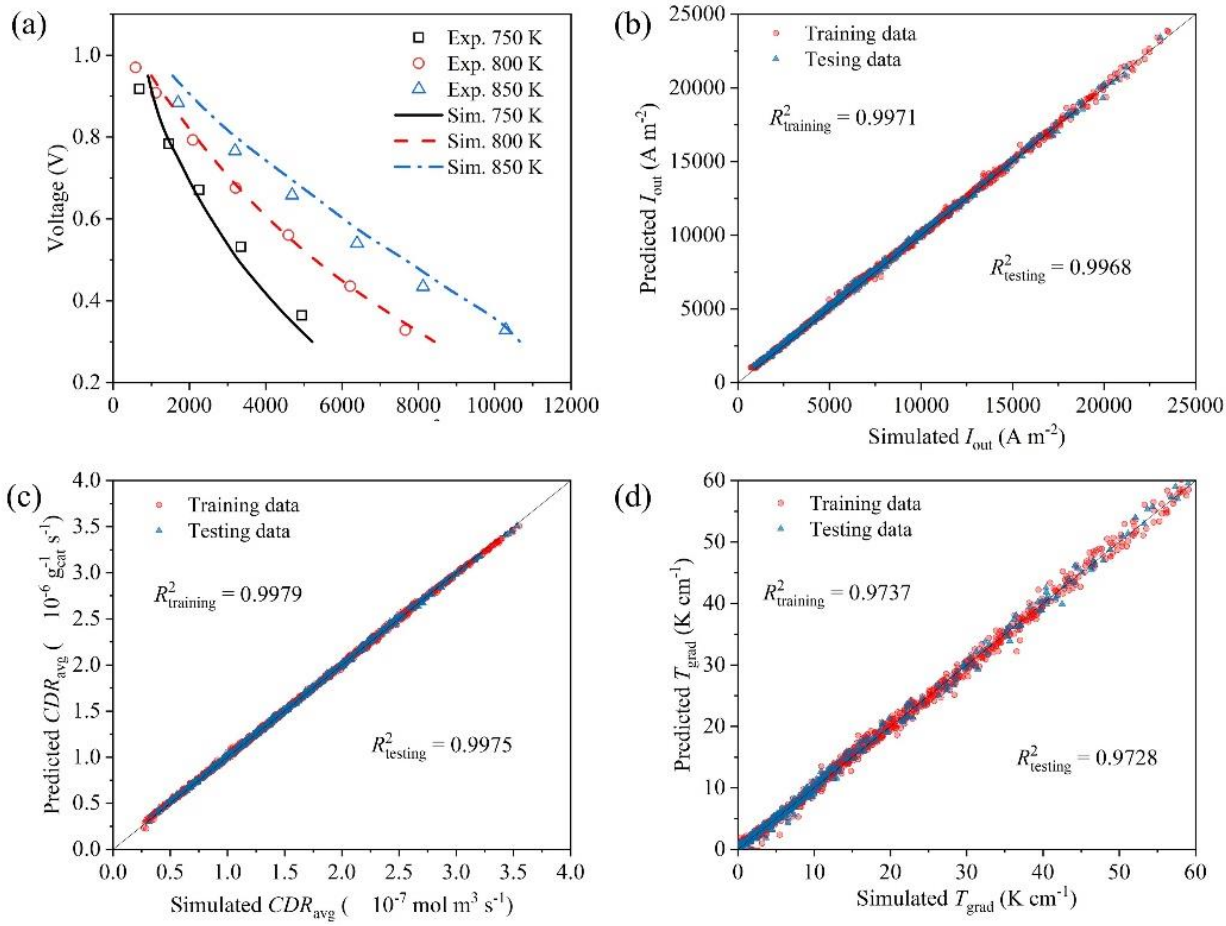

Fig. 2. Comparison of polarization curves between simulation results and experiment data (a). Comparison of predicted and simulated results for the training set and testing set: output current density (b), average carbon deposition rate (c), and maximum temperature gradient (d).

2.3 Deep-learning-based surrogate model

2.3.1 Deep neural network

Deep learning (DL) is a branch of artificial intelligence (AI) method based on the artificial neural network (ANN). Deep neural network (DNN), a biologically inspired computing scheme, can be considered as a stacked neural network with multiple layers. Like the biological neurons in the human brain, DNN consists of multiple sets of artificial neuron nodes, each of which combines the inputs linearly and passes the inputs through linear or nonlinear activation functions [39]. As a kind of black-box model, DNN has been shown to have the capability to

capture deep relationships between inputs and outputs in the absence of physical models [40]. The adopted DNN structure is shown in Fig. 1, which includes three hidden layers, as well as four inputs and three outputs. Each of the three hidden layers has 8 neurons. Four operating conditions that have a significant impact on electrochemical and carbon deposition performance are selected as inputs: steam/methane ratio (S/M), operating voltage (V_{op}), inlet fuel velocity (v_f), and operating temperature (T_{op}). In addition to the output current density (I_{out}) and the average carbon deposition rate (CDR_{avg}), the maximum temperature gradient (T_{grad}) is also used as an output parameter to evaluate the cell thermo-mechanical performance. Then, the deep learning-based surrogate model can be expressed as:

$$(I_{\text{out}},\ CDR_{\text{avg}},\ T_{\text{grad}}) = f(\text{S/M},\ V_{\text{op}},\ v_{\text{f}},\ T_{\text{op}}) \tag{14}$$

where the CDR_{avg} is one of the optimization criteria for the following multi-objective genetic algorithms which is calculated as the sum of carbon generation: $CDR_{\text{avg}} = R_{\text{MC}} + R_{\text{B}}$. Meanwhile, another optimization criteria, power density (P_{out}), is calculated as: $P_{\text{out}} = I_{\text{out}} V_{\text{op}}$. In addition, T_{grad} denotes the maximum temperature gradient along the flow direction, which is employed as an optimization constraint to characterize the thermal-mechanical endurance.

A total number of 1882×7 datasets is randomly split into a training set (80%) and a testing set (20%). The ranges of input parameters are shown in Table 3. The sizes of epoch and batch are 2000 and 32, respectively. The deep learning algorithm is implemented through Python 3.8. The DNN is constructed by Keras 2.4.3.

Table 3. Operating parameters as DNN inputs.

Parameters	Value
Steam/methane ratio (S/M)	1-4

Operating voltage (V_{op}, V)	0.4-0.8
Inlet fuel velocity (v_f, m s^{-1})	0.2-0.4
Operating tempearture (T_{op}, K)	1023-1173

2.3.2 Prediction performance

The root-mean square error (RMSE) and squared correlation coefficient (R^2) is chosen as the criteria to evaluate the prediction performance of the deep learning-based surrogate model:

$$\mathrm{RMSE} = \sqrt{\frac{1}{\mathrm{N}}\sum_{\mathrm{i=1}}^{\mathrm{N}}(x_{\mathrm{i}} - x_{\mathrm{i,p}})} \tag{15}$$

$$\mathrm{R}^2 = 1 - \frac{\sum_{\mathrm{i=1}}^{\mathrm{N}}(x_{\mathrm{i}} - x_{\mathrm{i,p}})^2}{\sum_{\mathrm{i=1}}^{\mathrm{N}}(x_{\mathrm{i}} - \overline{x}_{\mathrm{i}})^2} \tag{16}$$

where x_i is the simulation result using the multi-physics model; $x_{i,p}$ is the surrogate model predicted result; $\overline{x}_i$ is the mean value of multi-physics model simulated results. Fig. 2(b)-(c) show the comparison between simulated results and predicted results. The values of R^2 are also marked in the figure and are all larger than 0.97. The RMSE of the training set and testing set are 0.0184 and 0.0227 respectively and both remain at a low level. Also, there is no overfitting in the model. Therefore, the surrogate model has good prediction accuracy.

2.4 Global sensitivity analysis

The global sensitivity analysis aims at determining how uncertainty in different input parameters affects the final output of the model. It helps to understand the effects of individual physical quantities and the coupling of different physical quantities on the output parameters of a nonlinear complex model (such as a multi-physics fuel cell model). In this work, a variance-based sensitivity analysis called the Sobol method [41] is introduced to assess the importance of fuel cell operating conditions on output performance and carbon deposition. In

addition, the above DNN-trained surrogate model can perform fast prediction of cell performance, which also compensates for the drawback of the Sobol method which is computationally intensive.

According to the Sobol method, any physical model can be represented as: $y = f(\boldsymbol{x})$, where $\boldsymbol{x}$ is the vector of input parameters $\{x_1, x_2, \ldots, x_n\}$, y is the univariate model output. For the multi-physics SOFC model, $\boldsymbol{x}$ can be the operating conditions, and y is the related cell performance parameter. This function can be decomposed as follows:

$$y = f_0 + \sum_{i=1}^{d} f_i(x_i) + \sum_{i=1}^{d} f_{i,j}(x_i, x_j) + \ldots + f_{1,2,\ldots,d}(x_1, x_2, \ldots, x_d) \tag{17}$$

At the same time, the decomposition of total variance $V(y)$ can be expressed as:

$$V(y) = \sum_{i=1}^{k} V_i + \sum_{i \le j \le k} V_{ij} + \ldots + V_{1,2,\ldots,k} \tag{18}$$

where V_i, V_{ij}, …, $V_{1,2,\ldots,k}$ are the partial variances of f_i, f_{ij}, …, $f_{1,2,\ldots,k}$, respectively. Then the Sobol sensitivity index is stated as follows:

$$S_{i_1 \ldots i_k} = \frac{V_{i_1 \ldots i_k}}{V} \tag{19}$$

Here, the first-order sensitivity index S_i evaluates the importance of individual input parameter x_i on model output. The second-order sensitivity index S_{ij} evaluates the importance of the coupling of x_i and x_j. The input parameters selection and the range of values are the same as in the deep neural network section above. The global sensitivity analysis and multi-objective optimization program described below, are implemented through an in-house python code.

2.5 Optimization algorithm

For practical engineering problems, it is often necessary to optimize multiple objectives. There may be some conflict between these optimization objectives, meaning that improving one objective inevitably worsens the others [42]. The multi-physics optimization of SOFC is a typical nonlinear problem for which there is no single solution that can optimize each objective

simultaneously [43,44]. The multi-objective genetic objective algorithm has the capability to excavate the diverse region of solution space and is suitable for solving problems related to SOFC multi-objective optimization. The optimal solution set of MOGA (called Pareto optimum set) is illustrated in terms of the Pareto front, which is derived from the fitness function values in the objective space.

The optimization of DIR-SOFC in this work is focused on maximizing the power density (P_{out}) and minimizing the average carbon deposition region (CDR_{avg}), which are called objective functions. In practice, the amount of carbon deposited accumulates over time. Accordingly, we set the carbon deposition rate as an optimization criterion to obtain the best long-term performance. At the same time, the maximum allowable temperature gradient (T_{grad}) along the direction of the gas channel is used as a constraint. We can reasonably assume that the cell will not tolerate thermos-mechanical instability at levels below T_{grad}, and the cell performance does not deteriorate due to temperature gradients during the entire operation. The typical fuel cell operating conditions such as v_f, T_{op}, $V_{op,}$ and S/M are set as the decision variables. The optimization problem of DIR-SOFC can then be described as:

$$\begin{cases} Find\ the\ optimal\ solution\ X=\left\{\mathrm{S/M}, V_{op}, v_f, T_{op}\right\} \\ Max\ P_{out},\ Min\ CDR_{avg} \\ Subjected\ to\ \left\{T_{grad}\le T_{grad}^{Max}\right\} \end{cases} \tag{20}$$

The non-dominated sorting genetic algorithm-II (NSGA-II) with constraint-handling strategy is adopted to find the Pareto front in this work. The work flowchart of NSGA-II is shown in Fig. 1. The detailed procedure can be found in the original paper [45]. The DNN-trained surrogate model is employed in the calculation of fitness values. The integration of the surrogate model and NSGA-II can greatly accelerate the optimization process.

Besides, a decision-making method named TOPSIS (Technique for Order Preference by Similarity to an Ideal Solution) [46,47] is employed to select the optimal trade-off point. It is

vital to select the optimal solution from a variety of options for practical applications. However, because all solutions from the Pareto front have the same optimization level, it is hard to find the optimal alternative by sorting the fitness function values in the Pareto front. The TOPSIS chooses the options that are closest to the positive-ideal solution and the ones that are farthest away from the negative-ideal solution. The selection process of TOPSIS can be divided into several steps which are listed in Table 4.

Table 4. The TOPSIS selection process.

Step	Description	Variables and equations
Step 1	Create an evaluation matrix ($\left(x_{ij}\right)_{m\times n}$) with *m* alternatives and *n* objectives.	$\left(x_{ij}\right)_{m\times n}$
Step 2	Obtain the normalized matrix ($\left(r_{ij}\right)_{m\times n}$)	$r_{ij}=\frac{x_{ij}}{\sqrt{\sum_{i=1}^{m}x_{ij}^2}}$, $i=1,2,...,m,\ j=1,2,...,n$
Step 3	Multiply the weights (w_j) with the normalized matrix to form the weighted normalized matrix ($\left(v_{ij}\right)_{m\times n}$)	$v_{ij}=r_{ij}\times w_j$, $i=1,2,...,m,\ j=1,2,...,n$
Step 4	Determine the positive-ideal alternative (A^+) and the negative-ideal alternative (A^-)	$A^+=\begin{pmatrix}\min\left[v_{11},...v_{m1}\right],\min\left[v_{12},...v_{m2}\right],\\ ...,\min\left[v_{1n},...v_{mn}\right]\end{pmatrix}$ $A^-=\begin{pmatrix}\max\left[v_{11},...v_{m1}\right],\min\left[v_{12},...v_{m2}\right],\\ ...,\min\left[v_{1n},...v_{mn}\right]\end{pmatrix}$
Step 5	Calculate the distance between the target alternative and A^+ (d_i^+) and the distance between the target alternative and the A^- (d_i^-)	$d_i^+=\sqrt{\sum_{j=1}^{n}\left(v_{ij}-A_j^+\right)^2}$, $i=1,2,...,m,\ j=1,2,...,n$ $d_i^-=\sqrt{\sum_{j=1}^{n}\left(v_{ij}-A_j^-\right)^2}$, $i=1,2,...,m,\ j=1,2,...,n$

Step 6	Calculate the relative closeness to the ideal solution of alternatives (C_i)	$C_i = \frac{d_i^+}{d_i^+ + d_i^-}$, $i = 1, 2, ..., m$
Step 7	Rank the alternatives according to C_i, and the one shortest to the ideal solution is the optimal solution .	

3. Results and discussion

3.1 Results of sensitivity analysis

The global sensitivity analysis can help to clarify the input-output relationship and the multivariable interactions among the input parameters. Besides, a more reasonable parameter analysis can be performed based on the results of global sensitivity analysis. The first- and total-order of Sobol' indices are depicted as blue and red columns, respectively. The first-order Sobol' indices reflect the univariate effect of individual input parameters on the variance of outputs, while the total-order Sobol' indices represent both contributions of individual and interactive input parameters. We define individuals with the values of total-order Sobol' indices larger than 0.1 as the sensitive parameters. Furthermore, if the total-order Sobol' index of an individual is substantially larger than its first-order index, there will be higher-order interactions with other input parameters.

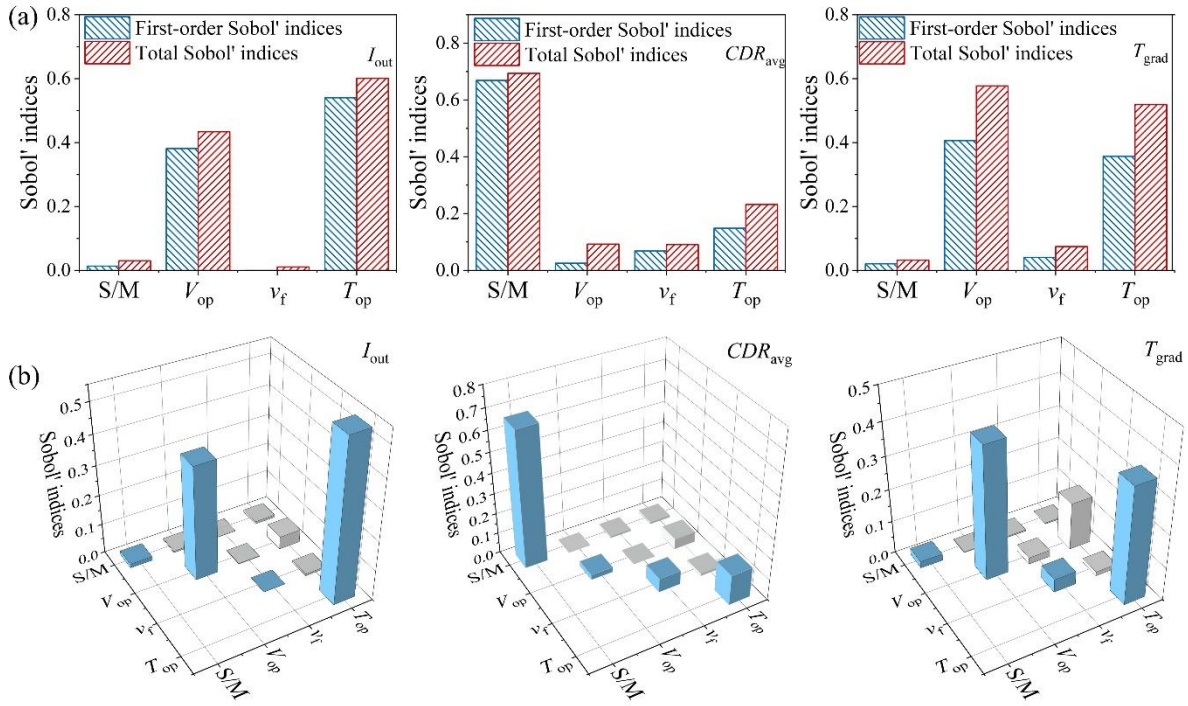

Fig. 3. Total, first-order (a) and second-order (b) Sobol' indices for the sensitive parameter.

As shown in Fig. 3(a), the sensitive parameters of output current density are V_{op} and T_{op}. The cell electrochemical performance is closely related to the V_{op} and T_{op}. For average carbon deposition rates, the sensitive parameters are S/M and T_{op}. This means that the effective way to minimize the carbon deposition rates is to control the steam/methane ratio and operating temperature. Both output current density and average carbon deposition rates exhibit strong first-order sensitivity to operating parameters. The contributions of different input parameters to the total variance are more complex for the maximum temperature gradient compared to the output current density and carbon deposition rates. The V_{op} and T_{op} have the most significant effect with high total-order indices of 0.406 and 0.357, respectively. The temperature gradient shows a lower sensitivity to S/M and v_f. Meanwhile, the univariate effects of four input parameters are insignificant. The differences between first- and total-order indices for temperature gradient are more remarkable, which highlights the interaction effects between each parameter. As depicted in Fig. 1(b), the contributions of two-parameter interactions are

plotted as 3D histograms. The first- and second-order indices are shown in blue and grey bars, respectively. For the output current density, the pairwise interaction of V_{op} and T_{op} shows a relatively minor influence with a lower second-order index (0.043). And the other pairwise interactions can be neglected. Similarly, the sensitive parameters exhibit some pairwise interactions for carbon deposition rates. The remarkable pairwise interactions between V_{op} and T_{op} suggest that it is more efficient to control these two parameters simultaneously to minimize the temperature gradient.

The global sensitivity analysis performed above can also provide effective strategies for parameter analysis. The operating voltage and temperature have significant effects on output current density and temperature gradient. For cell performance and carbon deposition rates, the effects of the univariate sensitive parameter will be of interest. The analysis on pairwise interaction effects will help to optimize the cell temperature distribution.

3.2 Parameter analysis

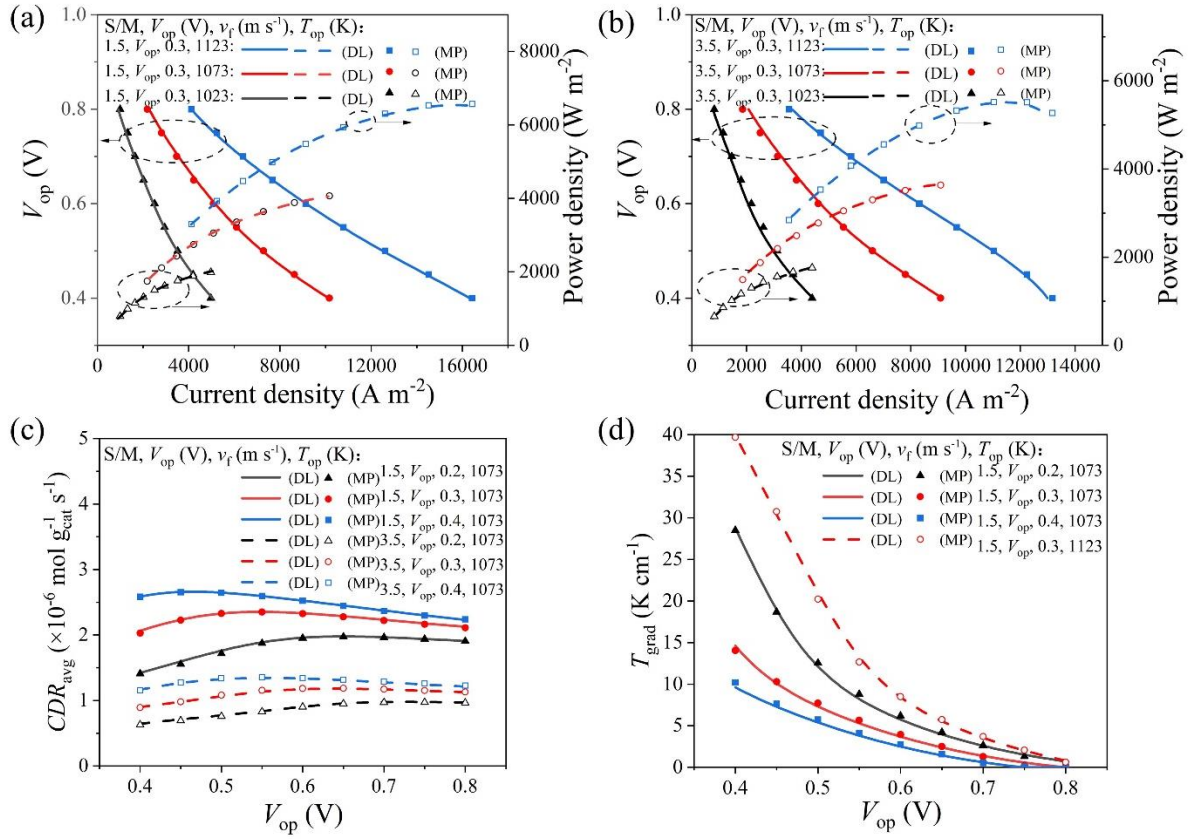

Fig. 4. The effects of sensitive parameters on cell performance (a) and (b), carbon deposition (c), and temperature gradient (d).

Based on the results of global sensitivity analysis, the effects of sensitive parameters on cell performance, carbon deposition, and temperature gradient obtained by the surrogate model are shown in Fig. 4. Meanwhile, some of the operating points calculated by the multi-physics model are plotted as controls. The results comparison between the multi-physics model and surrogate model proves the accuracy of the surrogate model in predicting the output parameters. Fig. 4(a) and (b) display the changes of current density-voltage and power density-voltage curves with the increase of operating temperature. For DIR-SOFC, the cell performance significantly increases with increasing temperature (Fig. 4(a)). When the operating temperature is increased from 1023 K to 1073 K and 1123 K, the maximum output power density is raised from 2019.4 W m^{-2} to 4051.0 W m^{-2} and 6540.8 W m^{-2}, respectively. At the same time, it is

found that under low operating voltage and high S/M conditions (Fig. 4(b)), the increment in current density slightly decreases at an operating temperature of 1123K, which will be discussed in the following section. The results of global sensitivity analysis reflect that the S/M significantly affects the carbon deposition rates, which is consistent with what is shown in Fig. 4(c). The larger S/M accelerates the methane steam reforming reaction and a higher methane conversion rate is beneficial to alleviate the carbon deposition [48]. At the same time, the overall average carbon deposition rates increase with the decreasing operating voltage and then decrease. That is, the decrease in operating voltage within a certain range leads to an increase in power density but also an increase in the amount of carbon deposition, meaning that there is a trade-off between cell performance and carbon deposition. This optimal operating point is the objective of the following multi-objective optimization work. The effects of sensitive parameters on the temperature gradient are shown in Fig. 4(d). The strong endothermic reforming reactions (MSR) result in a large temperature gradient along the cell length direction [49]. As the decrease of operating voltage, the accumulation of electrochemical heats increases the temperature gradient. For example, the maximum temperature gradient can be increased from 0.01 K cm^{-1} to 14.62 K cm^{-1} at an operating temperature of 1073 K and an inlet velocity of 0.3 m s^{-1}. Meanwhile, increasing the operating temperature will significantly increase the maximum temperature gradient. The combined effects of the chemical reaction heats, the electrochemical reaction heats, and the temperature distribution inside the cell are responsible for the above phenomenon and are discussed in detail below. Also, understanding this phenomenon helps to clarify the optimization objectives and improve the cell thermal performance.

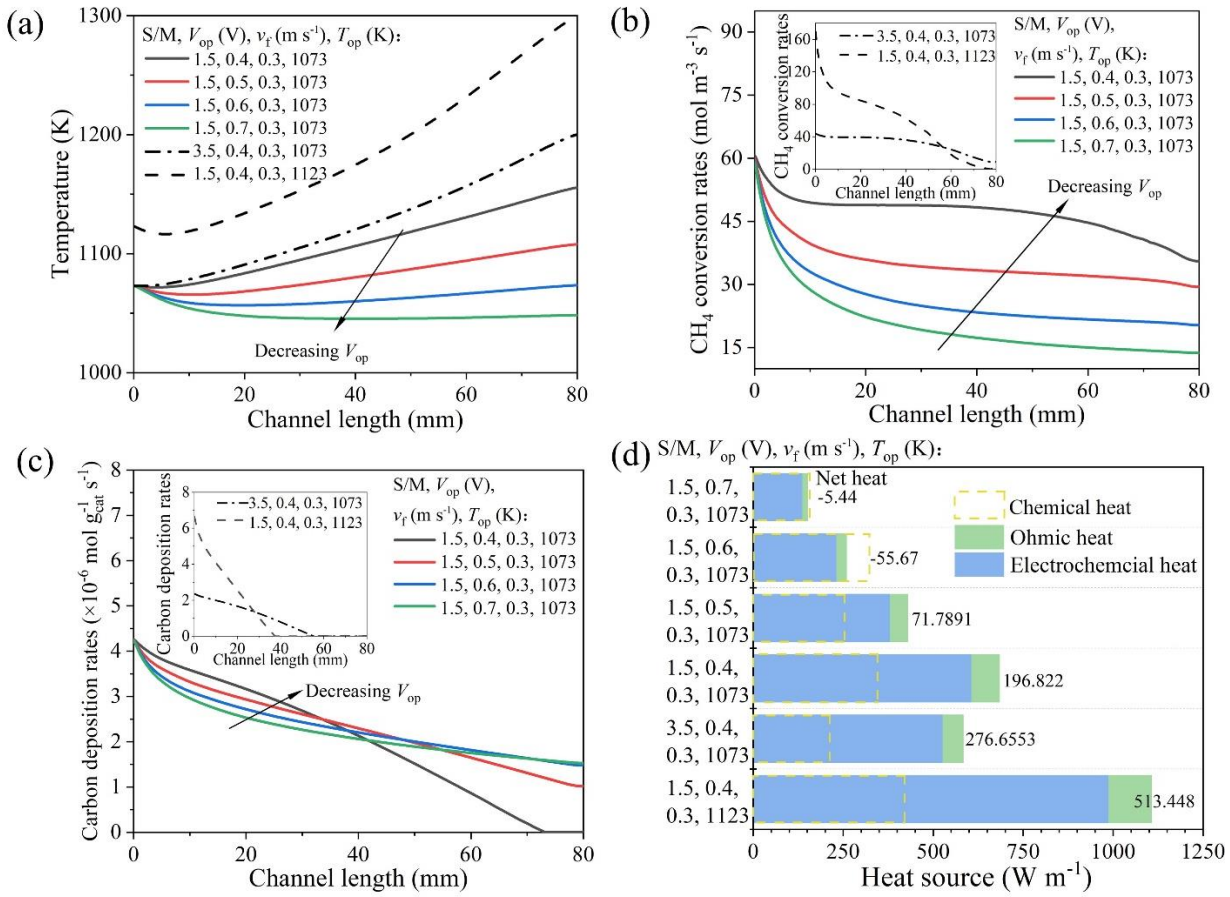

Fig. 5. Temperature (a), CH_4 conversion rates (b), and carbon deposition rates (c) distribution along the channel length direction obtained by the multi-physics model. Heat sources under different operating conditions (d).

In order to further clarify the effects of heat and mass transfer under different working conditions, the results obtained by the multi-physics model are depicted in Fig. 5. The overall temperature distribution significantly affects cell performance and carbon deposition. As shown in Fig. 5(a), the overall temperature gradually increases as the operating voltage decreases. The maximum temperature difference increases from 27.5 K at 0.7 V to 82.5 K at 0.4 V. At the same time, the increase of overall temperature also accelerates the methane conversion reaction (Fig. 5(b)), causing the overall methane conversion rates to increase with decreasing voltage. Higher temperature and lower voltage will accelerate the electrochemical

conversion of hydrogen and carbon monoxide to be more favorable for the methane conversion reaction. Fig. 5(c) shows the distribution of carbon deposition rates along the channel direction. Overall the carbon deposition rates decrease along the channel direction as the methane is gradually consumed. For lower V_{op} (0.4 V), the carbon deposition rate can be reduced to zero due to the complete consumption of methane. Besides, the chemical reaction heats, electrochemical reaction heats, and ohmic heats are plotted as stacked bars (Fig. 5(d)). It should be noted that the solid-filling part of each bar represents the electrochemical and ohmic exothermic heat for each operating condition. The dashed line represents the chemical endothermic heat. Both electrochemical and ohmic heats increase with the decrease of operating voltage. At higher V_{op} (0.7 and 0.6 V), the chemical heats are larger than the electrochemical and ohmic exothermic heats, the cell is in a state of heat absorption. As the further decreasing of V_{op}, the cell changes from heat absorption to an exothermic state. The value of net heat decreases from -5.44 W m^{-1} at 0.7 V to 196.8 W m^{-1} at 0.4 V. In addition to the effects of operating voltage, two cases considering the effects of operating temperature and S/M ratio are shown in Fig. 5(a). At lower operating voltage (0.4 V), increasing V_{op} causes the cell temperature distribution to show a trend of slightly decreasing and then increasing along the channel direction. The methane conversion rate also has a large increase, especially on the inlet side. At the same time, the values of the three kinds of heat have a large increase (Fig. 5(d)). In addition, increasing the S/M ratio has a significant effect on reducing carbon deposition. The above results are strongly correlated with the distribution of each gas component under the related condition and are discussed in the next section.

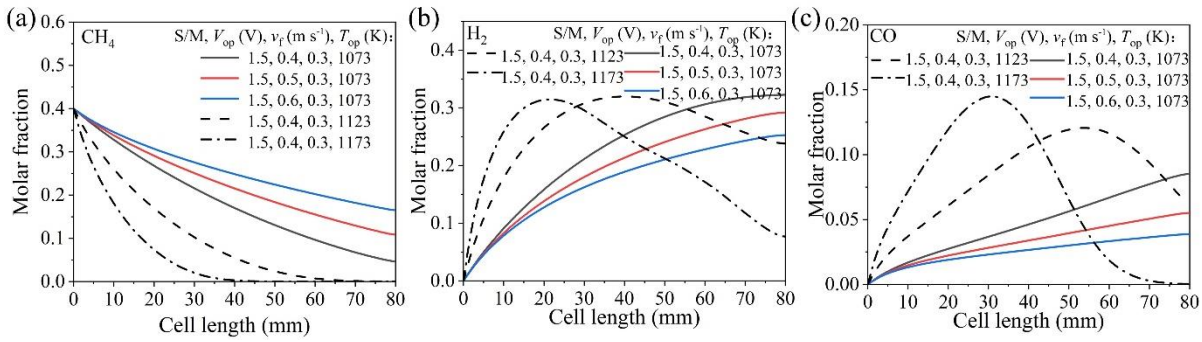

Fig. 6. Molar fraction distribution along channel length direction for CH_4 (a), H_2 (b), and CO (c).

Fig. 6(a), (b), and (c) represent the distribution of CH_4, H_2, and CO, respectively. As mentioned in the previous section, reducing V_{op} and increasing T_{op} are favorable for methane conversion. The molar fractions of H_2 and CO also increase along the channel length direction. By further increasing T_{op} to 1173 K, the methane is fully converted in the upstream region of the cell, and the molar fraction of H_2 and CO reaches a maximum and decreases in the subsequent range due to the consumption by electrochemical reactions. Recall from Fig. 5(a), when methane is converted rapidly, the electrochemical and ohmic heat in the downstream region is more than the chemical reaction heat absorption, resulting in a tendency for the cell temperature to slightly fall and then rise. This phenomenon is more pronounced for conditions where the methane is completely consumed. Then recall from Fig. 4(b), at higher T_{op} and larger S/M, less methane flux leads to complete conversion of methane. The H_2 and CO cannot maintain a high concentration or even drop in the second half of the cell (Fig. 6(b) and (c)). This is the reason for the small reduction in increment of current density at high temperatures and large S/M conditions in Fig. 4(b).

3.3 Results of multi-objective optimization

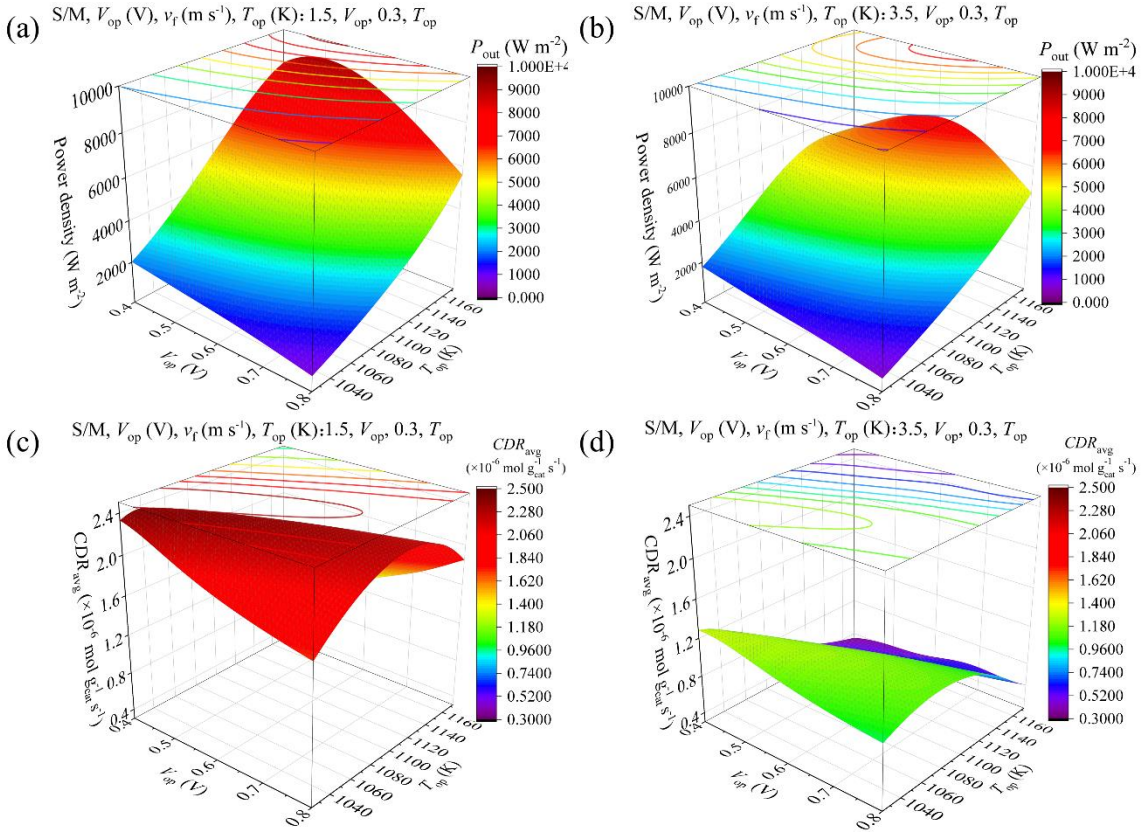

Fig. 7. Surface plots of surrogate model prediction: output power density with (a) low S/M ratio and (b) high S/M ratio; average carbon deposition rate (c) low S/M ratio and (d) high S/M ratio.

The results of the parametrical analysis above show that the cell performance and carbon deposition are influenced simultaneously by the various operating conditions. The surface plots obtained from the surrogate model are shown in Fig. 7, according to which the best combination of operating conditions for optimizing cell performance and carbon deposition can be quickly found. As shown in Fig. 7(a) and (b), at lower and higher S/M ratios (1.5 and 3.5), the maximum output power density can reach 9135.1 W m^{-2} and 6987.9 W m^{-2}, respectively. Meanwhile, the cell output power density is maximized at the lower operating voltage of 0.4-0.5 V. Decreasing V_{op} and increasing T_{op} can significantly improve cell performance. For carbon deposition (Fig. 7(c) and (d)), we can find that increasing S/M is an effective measure to inhibit carbon

deposition. The maximum carbon deposition rate of lower S/M (2.383×10^{-6}mol g_{cat}^{-1} s^{-1}) is about 1.9 times larger than that of higher S/M (1.284×10^{-6}mol g_{cat}^{-1} s^{-1}). It is evident that the method of enhancing cell performance may increase the risk of carbon deposition. Finding the trade-off between cell performance and carbon deposition through surface plots can be challenging.

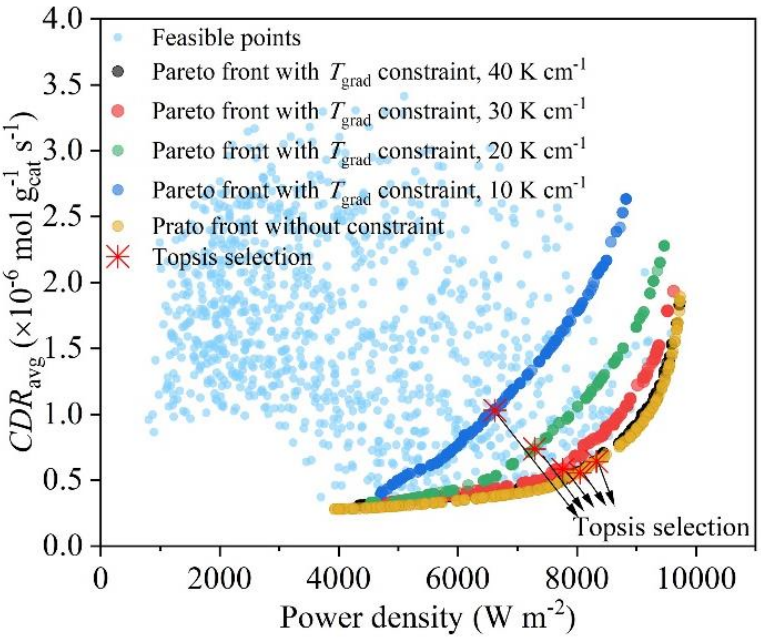

Fig. 8. Pareto fronts under different maximum temperature gradient constraints.

In this section, the deep learning-based surrogate model is implemented as the fitness function of MOGA. The trade-off (Pareto front) between output power density and carbon deposition rate for a given temperature gradient constraint is depicted in Fig. 8. The non-uniform distribution will raise a critical challenge to the thermal management of cells and stack. The temperature gradient causes thermal stress, and the excessively high temperature facilitates the coarsening process of Ni particles which is not desirable to long-term cell stability [18]. To prevent thermomechanical failure, the maximum temperature gradient should not exceed 10 K

cm^{-1} [50]. The weights assigned to output power density and carbon deposition rate in the TOPSIS selection process are 0.7 and 0.3, respectively.

As the temperature gradient constraint decreases, the cell operating on the Pareto front suffers both a decrease in performance and more severe carbon deposition. The maximum power densities on the Pareto fronts are 8823.42 W m^{-2} (10 K cm^{-1}), 9467.2 W m^{-2} (20 K cm^{-1}), 9625.3 W m^{-2} (30 K cm^{-1}), 9729.3 W m^{-2} (40 K cm^{-1}) and 9731.0 W m^{-2} (no constraint), respectively. The minimum average carbon deposition rates on the Pareto fronts for different temperature gradient constraints are very close. This multi-objective optimization framework can be used to achieve good performance output and resistance to carbon deposition during operation while maintaining a small temperature gradient (<10 K cm^{-1}) by adopting the operating conditions on the Pareto fronts. Under different constraints, the working points selected by TOPSIS and their output parameters are listed in Table 5. The maximum output power density on the Pareto fronts can reach 9731.0 W m^{-2} with no temperature gradient constraint, but the average carbon deposition rate has also reached 1.89×10^{-6}mol g_{cat}^{-1} s^{-1}. For the TOPSIS selection of 10 K cm^{-1} constraint, the output power density is 6618.9 W m^{-2}, and the average carbon deposition rate is 1.03×10^{-6}mol g_{cat}^{-1} s^{-1}. From the results of TOPSIS selection, it is possible to sacrifice 32.0% of cell performance to achieve a 45.5% reduction in carbon deposition, while ensuring that the maximum temperature gradient is within 10 K cm^{-1}. The results show that a temperature gradient control of 10 K cm^{-1} can be achieved using this optimization framework, which can further be applied to the real-time control of DIR-SOFC to regulate the temperature gradient in real-time and obtain optimal performance simultaneously.

Table 5. The parameters of optimal working points are selected by TOPSIS.

	10 K cm^{-1}	20 K cm^{-1}	30 K cm^{-1}	40 K cm^{-1}	No

					constraint
S/M	2.63	3.19	3.58	3.0	3.31
V_{op} (V)	0.708	0.647	0.580	0.407	0.490
v_f (m s^{-1})	0.399	0.398	0.398	0.4	0.4
T_{op} (K)	1173	1173	1173	1173	1173
P_{out} (W m^{-2})	6618.9	7288.7	7761.3	8328.2	8049.3
CDR_{avg} ($\times 10^{-6}$mol g_{cat}^{-1} s^{-1})	1.030	0.737	0.584	0.641	0.556
T_{grad} (K cm^{-1})	9.1	19.9	29.8	39.3	44.1

Conclusions

In this study, a novel framework for optimizing the electrochemistry and carbon deposition performance of DIR-SOFC is proposed. A multi-physics model is established to perform parameter analysis and generate a dataset. The dataset is then used to train a deep neural network (DNN) which acts as a surrogate model. The surrogate model can quickly and accurately predict cell output performance, carbon deposition rates, and maximum temperature gradient. Based on the surrogate model, the Sobol method and NSGA-II are applied to perform the global sensitivity analysis and the multi-objective optimization. Based on the multi-objective optimization results, the resulting operating conditions can be selected to achieve real-time control of cell performance, carbon deposition, and temperature during the actual operation of the DIR-SOFC. The proposed optimization framework can be extended to other aspects of SOFC optimization, such as training neural networks to rapidly obtain electrode performance under different microstructures and using multi-objective optimization to obtain electrode microstructures for optimal performance and durability. The above workflow can also

be applied in other energy conversion devices to achieve fast multi-objective optimization. The major findings and conclusions are listed below:

(1) The electrochemical performance of the cell is mainly affected by the univariate changes of operating voltage and temperature. Carbon deposition is influenced by the univariate changes of steam/methane ratio and operating temperature. The maximum temperature gradient is mainly the result of the pairwise interactions of operating voltage and operating temperature. In other words, the most effective way to improve thermomechanical performance is to adjust all the two sensitive parameters simultaneously.

(2) The maximum power density is usually generated at lower operating voltages, but this condition causes a large temperature gradient. As the decrease of operating voltage, the accumulation of electrochemical heats will increase the temperature gradient. Meanwhile, the overall temperature distribution and steam/methane ratio play a crucial role in the carbon deposition rates. There is a trade-off between carbon deposition and cell output performance. Reducing carbon deposition often comes at the cost of some cell performance.

(3) The Pareto fronts under different temperature gradient constraints are obtained by the multi-objective genetic algorithms (MOGA). This optimization tool achieves a significant reduction in carbon deposition rates while maintaining a high output power density and a safe maximum temperature gradient (<10 K cm^{-1}).

Acknowledgements

This work is supported by the National Natural Science Foundation of China (Grant No. 51976138). M. NI also thanks to the grants (Project Number: PolyU 152064/18E and N_PolyU552/20) from Research Grant Council, University Grants Committee, Hong Kong SAR.

References

[1] Bao C, Wang Y, Feng D, et al. Macroscopic modeling of solid oxide fuel cell (SOFC) and model-based control of SOFC and gas turbine hybrid system. Progress in Energy and Combustion Science, 2018, 66: 83-140. https://doi.org/10.1016/j.pecs.2017.12.002.

[2] Wachsman E D, Lee K T. Lowering the temperature of solid oxide fuel cells. Science, 2011, 334(6058): 935-939. https://10.1126/science.1204090.

[3] Cottrell C A, Grasman S E, Thomas M, et al. Strategies for stationary and portable fuel cell markets. International Journal of Hydrogen Energy, 2011, 36(13): 7969-7975. https://doi.org/10.1016/j.ijhydene.2011.01.056.

[4] Prakash B S, Kumar S S, Aruna S T. Properties and development of Ni/YSZ as an anode material in solid oxide fuel cell: a review. Renewable and Sustainable Energy Reviews, 2014, 36: 149-179. https://doi.org/10.1016/j.rser.2014.04.043.

[5] Kupecki J, Papurello D, Lanzini A, et al. Numerical model of planar anode supported solid oxide fuel cell fed with fuel containing H_2S operated in direct internal reforming mode (DIR-SOFC). Applied Energy, 2018, 230: 1573-1584. https://doi.org/10.1016/j.apenergy.2018.09.092.

[6] Lanzini A, Leone P, Guerra C, et al. Durability of anode supported Solid Oxides Fuel Cells (SOFC) under direct dry-reforming of methane. Chemical Engineering Journal, 2013, 220: 254-263. https://doi.org/10.1016/j.cej.2013.01.003.

[7] Babaei A, Li J. Electrocatalytic promotion of palladium nanoparticles on hydrogen oxidation on Ni/GDC anodes of SOFCs via spillover. Journal of the Electrochemical Society, 2009, 156(9): B1022. https://doi.org/10.1149/1.3156637.

[8] Xie H, Zhai S, Chen B, et al. Coal pretreatment and Ag-infiltrated anode for high-performance hybrid direct coal fuel cell. Applied Energy, 2020, 260: 114197. https://doi.org/10.1016/j.apenergy.2019.114197.

[9] Horita T, Yamaji K, Kato T, et al. Design of metal/oxide interfaces for the direct introduction of hydrocarbons into SOFCs. Journal of Power Sources, 2004, 131(1-2): 299-303. https://doi.org/10.1016/j.jpowsour.2003.10.018.

[10] Hua B, Li M, Chi B, et al. Enhanced electrochemical performance and carbon deposition resistance of Ni–YSZ anode of solid oxide fuel cells by in situ formed Ni–MnO layer for CH_4 on-cell reforming. Journal of Materials Chemistry A, 2014, 2(4): 1150-1158. https://doi.org/10.1039/C3TA12766D.

[11] Girona K, Laurencin J, Fouletier J, et al. Carbon deposition in CH_4/CO_2 operated SOFC: Simulation and experimentation studies. Journal of Power Sources, 2012, 210: 381-391. https://doi.org/10.1016/j.jpowsour.2011.12.005.

[12] Gholaminezhad I, Paydar M H, Jafarpur K, et al. Multi-scale mathematical modeling of methane-fueled SOFCs: Predicting limiting current density using a modified Fick's model. Energy Conversion and Management, 2017, 148: 222-237. https://doi.org/10.1016/j.enconman.2017.05.071.

[13] Gür T M. Comprehensive review of methane conversion in solid oxide fuel cells: prospects for efficient electricity generation from natural gas. Progress in Energy and Combustion Science, 2016, 54: 1-64. https://doi.org/10.1016/j.pecs.2015.10.004.

[14] Muramoto A, Kikuchi Y, Tachikawa Y, et al. High-pressure CHO diagrams: Fuel composition, carbon deposition, and open circuit voltage of pressurized SOFCs. International Journal of Hydrogen Energy, 2017, 42(52): 30769-30786. https://doi.org/10.1016/j.ijhydene.2017.10.122.

[15] Subotić V, Baldinelli A, Barelli L, et al. Applicability of the SOFC technology for coupling with biomass-gasifier systems: Short-and long-term experimental study on SOFC performance and degradation behaviour. Applied Energy, 2019, 256: 113904. https://doi.org/10.1016/j.apenergy.2019.113904.

[16] Wang Y, Yoshiba F, Kawase M, et al. Performance and effective kinetic models of methane steam reforming over Ni/YSZ anode of planar SOFC. International Journal of Hydrogen Energy, 2009, 34(9): 3885-3893. https://doi.org/10.1016/j.ijhydene.2009.02.073.

[17] Schluckner C, Subotić V, Lawlor V, et al. Three-dimensional numerical and experimental investigation of an industrial-sized SOFC fueled by diesel reformat–Part II: Detailed reforming chemistry and carbon deposition analysis. International Journal of Hydrogen Energy, 2015, 40(34): 10943-10959. https://doi.org/10.1016/j.ijhydene.2015.06.024.

[18] Wang Y, Wu C, Du Q, et al. Morphology and performance evolution of anode microstructure in solid oxide fuel cell: A model-based quantitative analysis. Applications in Energy and Combustion Science, 2021, 5: 100016. https://doi.org/10.1016/j.jaecs.2020.100016.

[19] Wang Y, Du Y, Ni M, et al. Three-dimensional modeling of flow field optimization for co-electrolysis solid oxide electrolysis cell. Applied Thermal Engineering, 2020, 172: 114959. https://doi.org/10.1016/j.applthermaleng.2020.114959.

[20] Guo M, Xiao G, Wang J, et al. Parametric study of kW-class solid oxide fuel cell stacks fueled by hydrogen and methane with fully multiphysical coupling model. International Journal of Hydrogen Energy, 2021, 46(14): 9488-9502. https://doi.org/10.1016/j.ijhydene.2020.12.092.

[21] Beale S B, Choi H W, Pharoah J G, et al. Open-source computational model of a solid oxide fuel cell. Computer physics communications, 2016, 200: 15-26. https://doi.org/10.1016/j.cpc.2015.10.007.

[22] Al Moussawi H, Fardoun F, Louahlia H. 4-E based optimal management of a SOFC-CCHP system model for residential applications. Energy Conversion and Management, 2017, 151: 607-629. https://doi.org/10.1016/j.enconman.2017.09.020.

[23] Wu X, Xu Y W, Xue T, et al. Health state prediction and analysis of SOFC system based

on the data-driven entire stage experiment. Applied energy, 2019, 248: 126-140. https://doi.org/10.1016/j.apenergy.2019.04.053.

[24] Mozdzierz M, Brus G, Sciazko A, et al. Towards a thermal optimization of a methane/steam reforming reactor. Flow, Turbulence and Combustion, 2016, 97(1): 171-189. https://doi.org/10.1007/s10494-015-9693-2.

[25] Grzegorz B, Komatsu Y, Kimijima S, et al. An analysis of biogas reforming process on Ni/YSZ and Ni/SDC catalysts. International Journal of Thermodynamics, 2012, 15(1): 43-51. https://doi.org/10.5541/ijot.315.

[26] Sciazko A, Komatsu Y, Brus G, et al. A novel approach to the experimental study on methane/steam reforming kinetics using the Orthogonal Least Squares method. Journal of Power Sources, 2014, 262: 245-254. https://doi.org/10.1016/j.jpowsour.2014.03.097.

[27] Chalusiak M, Wrobel M, Mozdzierz M, et al. A numerical analysis of unsteady transport phenomena in a Direct Internal Reforming Solid Oxide Fuel Cell. International Journal of Heat and Mass Transfer, 2019, 131: 1032-1051. https://doi.org/10.1016/j.ijheatmasstransfer.2018.11.113

[28] Brus G, Raczkowski P F, Kishimoto M, et al. A microstructure-oriented mathematical model of a direct internal reforming solid oxide fuel cell. Energy Conversion and Management, 2020, 213: 112826. https://doi.org/10.1016/j.enconman.2020.112826.

[29] Tai X Y, Zhang H, Niu Z, et al. The future of sustainable chemistry and process: Convergence of artificial intelligence, data and hardware. Energy and AI, 2020: 100036. https://doi.org/10.1016/j.egyai.2020.100036.

[30] Pajak M, Buchaniec S, Kimijima S, et al. A multiobjective optimization of a catalyst distribution in a methane/steam reforming reactor using a genetic algorithm. international journal of hydrogen energy, 2021, 46(38): 20183-20197. https://doi.org/10.1016/j.ijhydene.2020.02.228.

[31] Pajak M, Brus G, Szmyd J S. Genetic algorithm-based strategy for the steam reformer optimization. International Journal of Hydrogen Energy, 2021. https://doi.org/10.1016/j.ijhydene.2021.10.046.

[32] Koncewicz W, Moździerz M, Brus G. A fast Gaussian process-based method to evaluate carbon deposition during hydrocarbons reforming. International Journal of Hydrogen Energy, 2021. https://doi.org/10.1016/j.ijhydene.2021.07.213.

[33] Zhan R, Wang Y, Ni M, et al. Three-dimensional simulation of solid oxide fuel cell with metal foam as cathode flow distributor. International Journal of Hydrogen Energy, 2020, 45(11): 6897-6911. https://doi.org/10.1016/j.ijhydene.2019.11.221.

[34] Wang Y, Zhan R, Qin Y, et al. Three-dimensional modeling of pressure effect on operating characteristics and performance of solid oxide fuel cell. International Journal of Hydrogen Energy, 2018, 43(43): 20059-20076. https://doi.org/10.1016/j.ijhydene.2018.09.025.

[35] Ni M. Modeling and parametric simulations of solid oxide fuel cells with methane carbon dioxide reforming. Energy Conversion and Management, 2013, 70: 116-129. https://doi.org/10.1016/j.enconman.2013.02.008.

[36] Fan P, Zhang X, Hua D, et al. Experimental study of the carbon deposition from CH_4 onto the Ni/YSZ anode of SOFCs. Fuel Cells, 2016, 16(2): 235-243. https://doi.org/10.1002/fuce.201500038.

[37] Hua D, Li G, Lu H, et al. Investigation of carbon formation on Ni/YSZ anode of solid oxide fuel cell from CO disproportionation reaction. International Communications in Heat and Mass Transfer, 2018, 91: 23-29. https://doi.org/10.1016/j.icheatmasstransfer.2017.11.014.

[38] Li C, Shi Y, Cai N. Elementary reaction kinetic model of an anode-supported solid oxide fuel cell fueled with syngas. Journal of Power Sources, 2010, 195(8): 2266-2282. https://doi.org/10.1016/j.jpowsour.2009.10.051.

[39] Alkhayat G, Mehmood R. A review and taxonomy of wind and solar energy forecasting methods based on deep learning. Energy and AI, 2021: 100060. https://doi.org/10.1016/j.egyai.2021.100060.

[40] LeCun Y, Bengio Y, Hinton G. Deep learning. nature, 2015, 521(7553): 436-444. https://doi.org/10.1038/nature14539

[41] Sobol I M. Global sensitivity indices for nonlinear mathematical models and their Monte Carlo estimates. Mathematics and computers in simulation, 2001, 55(1-3): 271-280. https://doi.org/10.1016/S0378-4754(00)00270-6.

[42] Marler R T, Arora J S. Survey of multi-objective optimization methods for engineering. Structural and multidisciplinary optimization, 2004, 26(6): 369-395. https://doi.org/10.1007/s00158-003-0368-6.

[43] Yan Z, He A, Hara S, et al. Modeling of solid oxide fuel cell (SOFC) electrodes from fabrication to operation: Microstructure optimization via artificial neural networks and multi-objective genetic algorithms. Energy Conversion and Management, 2019, 198: 111916. https://doi.org/10.1016/j.enconman.2019.111916.

[44] Gholaminezhad I, Jafarpur K, Paydar M H, et al. Multi-scale multi-objective optimization and uncertainty analysis of methane-fed solid oxide fuel cells using Monte Carlo simulations. Energy Conversion and Management, 2017, 153: 175-187. https://doi.org/10.1016/j.enconman.2017.10.011.

[45] Deb K, Pratap A, Agarwal S, et al. A fast and elitist multiobjective genetic algorithm: NSGA-II. IEEE transactions on evolutionary computation, 2002, 6(2): 182-197. https://doi.org/10.1109/4235.996017.

[46] Behzadian M, Otaghsara S K, Yazdani M, et al. A state-of the-art survey of TOPSIS applications. Expert Systems with applications, 2012, 39(17): 13051-13069. https://doi.org/10.1016/j.eswa.2012.05.056.

[47] Wang T H, Wu H C, Meng J H, et al. Optimization of a double-layered microchannel heat sink with semi-porous-ribs by multi-objective genetic algorithm. International Journal of Heat and Mass Transfer, 2020, 149: 119217. https://doi.org/10.1016/j.ijheatmasstransfer.2019.119217.

[48] Lyu Z, Shi W, Han M. Electrochemical characteristics and carbon tolerance of solid oxide 40fuel cells with direct internal dry reforming of methane. Applied Energy, 2018, 228: 556-567. https://doi.org/10.1016/j.apenergy.2018.06.114.

[49] Zeng Z, Qian Y, Zhang Y, et al. A review of heat transfer and thermal management methods for temperature gradient reduction in solid oxide fuel cell (SOFC) stacks. Applied Energy, 2020, 280: 115899. https://doi.org/10.1016/j.apenergy.2020.115899.

[50] Atkinson A, Selcuk A. Mechanical behaviour of ceramic oxygen ion-conducting membranes. Solid State Ionics, 2000, 134(1-2): 59-66. https://doi.org/10.1016/S0167-2738(00)00714-1.